Assimilation of Doppler Radar Observations with an Ensemble Square Root Filter: A Squall Line Case Study

QIN Yanyan[1,2]* (秦琰琰), GONG Jiandong[3] (龚建东), LI Zechun[4] (李泽椿), and SHENG Rifeng[5] (盛日锋)

1 *National Marine Environment Forecast Center, Beijing* 100081

2 *Key Laboratory of Research on Marine Hazards Forecasting, National Marine Environmental Forecast Center, Beijing* 100081

3 *Center for Numerical Weather Prediction, CMA, Beijing* 100081

4 *National Meteorological Center, CMA, Beijing* 100081

5 *Weather Modification Office of People's Government of Shandong, Jinan* 250031

ABSTRACT

The effectiveness of using an Ensemble Square Root Filter (EnSRF) to assimilate real Doppler radar observations on convective scale is investigated by applying the technique to a case of squall line on 12 July 2005 in midwest Shandong Province using the Weather Research and Forecasting (WRF) model. The experimental results show that: (1) The EnSRF system has the potential to initiate a squall line accurately by assimilation of real Doppler radar data. The convective-scale information has been added into the WRF model through radar data assimilation and thus the analyzed fields are improved noticeably. The model spin-up time has been shortened, and the precipitation forecast is improved accordingly. (2) Compared with the control run, the deterministic forecast initiated with the ensemble mean analysis of EnSRF produces more accurate prediction of microphysical fields. The predicted wind and thermal fields are reasonable and in accordance with the characteristics of convective storms. (3) The propagation direction of the squall line from the ensemble mean analysis is consistent with that of the observation, but the propagation speed is larger than the observed. The effective forecast period for this squall line is about 5–6 h, probably because of the nonlinear development of the convective storm.

Key words: radar data assimilation, ensemble square root filter, squall line

Citation: Qin Yanyan, Gong Jiandong, Li Zechun, et al., 2014: Assimilation of Doppler radar observations with an ensemble square root filter: A squall line case study. *J. Meteor. Res.*, **28**(2), 230–251, doi: 10.1007/s13351-014-2046-6.

1. Introduction

Numerical weather prediction (NWP) is an initial and boundary condition problem. Accurate and balanced initial estimate of the atmospheric state is essential to the improvement of the NWP. With high spatial and temporal resolutions, Doppler radar data are increasingly used to initialize the convective-scale NWP, which plays a key role in improving the accuracy of early warning of disastrous weather on convective scale. With establishment of the NEXRAD network in China, there has been a rapid growth in the radar detection capability, data coverage, and data quality, which provides advantageous conditions for assimilation of radar data. The continuous development of data assimilation techniques and computing power in recent years makes it possible to assimilate Doppler radar data in high-resolution nonhydrostatic numerical models.

The way of assimilating radar data mainly includes thermodynamic retrieval (Gal-Chen, 1978; Hane and Ray, 1985), thermodynamic initialization (Lin et al., 1993; Xue et al., 1998; Zhang et al., 1998), nudging (Jones and Macpherson, 1997), three- or four-

dimensional variational method (Sun and Crook, 1997; Xu et al., 2004; Yang Yanrong et al., 2008; Yang Yi et al., 2008; Xu et al., 2012), and Ensemble Kalman Filter (EnKF). EnKF is based on the Monte Carle idea, which utilizes a group of short-term ensemble forecasts to estimate the background error covariance. EnKF has been implemented in various atmospheric and oceanic models due to its advantages of flow-dependent background error covariance, nonlinear model and observation operator, no need for tangent linear and adjoint models, and easy parallelization (e.g., Yang et al., 2011). Since first introduced into the geophysical field by Evensen (1994), EnKF has become one of the most promising assimilation methods. In recent years, considerable progress has been made in exploring the potential of using EnKF to assimilate radar data on convective scale. As for simulated radar data assimilation, many studies focused on analyses of flow field and thermodynamic and microphysical fields through the observing system simulation experiments (OSSEs). These experimental studies have demonstrated the feasibility and effectiveness of EnKF on storm scales (Snyder and Zhang, 2003; Zhang et al., 2004; Tong and Xue, 2005; Xu et al., 2006; Xue et al., 2006; Qin et al., 2012; Xu et al., 2012; Xue and Dong, 2013). However, there are few such kind of studies conducted in China.

As for real radar data assimilation, Dowell et al. (2004) explored for the first time the feasibility of using an EnKF on storm scale. In their study, 10 successive volumes of a single radar radial velocity and reflectivity observations over a period of 47 min were assimilated into a three-dimensional warm cloud model developed by Sun and Crook (1997) by using an Ensemble Square Root Filter (EnSRF). Retrievals of wind fields were generally correct, while the low-level cold pool was too strong compared with the observation, probably due to model errors and observational limitations. Xu et al. (2006) used the same model to assimilate six successive volumes of radial velocity and rain water retrieved from reflectivity of Yichang-Jingzhou dual Doppler radar. Their study shows that by using the EnKF technique, the wind fields together with

thermodynamic and microphysical fields of a convective heavy rainfall system can be well retrieved. However, the model used in the above studies is a warm cloud model, which does not include the ice microphysics. Only rain water mixing ratio is updated in the analysis, while the retrieval of ice-phase hydrometeor fields is not included. The ice-phase hydrometeors actually exist and play an important role in exuberant convective cells (Hu et al., 1998). In addition, previous studies assimilating real radar data with EnKF only focus on the accuracy of retrieved fields, instead of assessing the performance of forecasts initialized by analyzed fields.

In this study, the performance of the EnSRF technique is examined by applying it to the assimilation of real radar data during a squall line event on 12 July 2005 in midwest of Shandong Province using the Weather Research and Forecasting (WRF) model with a complex multiclass ice microphysics scheme. A deterministic prediction is also made using the ensemble mean of the third assimilation cycle as the initial condition. All variables including ice species are updated in our analysis, and we concern not only the accuracy of retrieved state of the storm, but also the accuracy of prediction from this retrieved state.

2. EnSRF technique and assimilation system

In the standard EnKF formulation, observations are treated as random variables that are subject to added perturbations (Houtekamer and Mitchell, 1998), which will cause sampling errors associated with the use of perturbed observations. The EnSRF method, which does not perturb observations, is designed by Whitaker and Hamill (2002) to avoid the issue. They demonstrated that EnSRF produces an analysis ensemble with mean error lower than that of EnKF for the same ensemble size. The comparison was done in a Lorenz model and a two-level idealized general circulation model (GCM).

Similar to other ensemble-based Kalman filters, the EnSRF algorithm has two steps: integration and analysis. At the integration step, a set of short-term

ensemble forecasts are performed; while at the analysis step, background error covariance is estimated from this ensemble, and then the ensemble is updated. The updated ensemble is integrated forward until new observations are available again and the sequential data assimilation cycle is repeated. EnSRF is distinctive in that the ensemble mean ($\bar{\mathbf{x}}^\mathrm{a}$) and the deviations of ensemble members from the mean ($\mathbf{x}'^\mathrm{a}$) are updated separately. Under the assumption of independence of observations, the order in which we assimilate them is irrelevant. Observations are analyzed serially, until all the observations are assimilated.

The analysis equation for ensemble mean state is:

$$\bar{\mathbf{x}}^\mathrm{a} = \bar{\mathbf{x}}^\mathrm{f} + \boldsymbol{K}(\mathbf{y}^\mathrm{o} - \boldsymbol{H}\bar{\mathbf{x}}^f), \tag{1}$$

in which the superscripts a and f denote analysis and forecast, respectively; $\boldsymbol{H}$ is observation operator that projects model state to observation $\mathbf{y}^\mathrm{o}$, and $\boldsymbol{K}$ is the Kalman gain matrix:

$$\boldsymbol{K} = \boldsymbol{P}^\mathrm{f}\boldsymbol{H}^\mathrm{T}(\boldsymbol{H}\boldsymbol{P}^\mathrm{f}\boldsymbol{H}^\mathrm{T} + \boldsymbol{R})^{-1}, \tag{2}$$

where $\boldsymbol{R}$ is observation error covariance matrix, $\boldsymbol{H}$ is the Jacobean matrix of $\boldsymbol{H}$, and $\boldsymbol{P}^\mathrm{f}$ is prior error covariance matrix which in practice does not need to be calculated explicitly in the EnSRF algorithm, while the background error covariance $\boldsymbol{P}^\mathrm{f}\boldsymbol{H}^\mathrm{T}$ and $\boldsymbol{H}\boldsymbol{P}^\mathrm{f}\boldsymbol{H}^\mathrm{T}$ are estimated according to

$$\boldsymbol{P}^\mathrm{f}\boldsymbol{H}^\mathrm{T} = \rho^\mathrm{o}\left[\frac{1}{N-1}\sum_{k=1}^{N}(x_k^\mathrm{f} - \bar{x}^\mathrm{f})(\boldsymbol{H}(x_k^\mathrm{f}) \right.$$
$$\left. -\overline{\boldsymbol{H}(x^\mathrm{f})})^\mathrm{T}\right], \tag{3}$$

$$\boldsymbol{H}\boldsymbol{P}^\mathrm{f}\boldsymbol{H}^\mathrm{T} = \frac{1}{N-1}\sum_{k=1}^{N}(\boldsymbol{H}(x_k^\mathrm{f}) - \overline{\boldsymbol{H}(x^\mathrm{f})})$$
$$\cdot(\boldsymbol{H}(x_k^\mathrm{f}) - \overline{\boldsymbol{H}(x^\mathrm{f})})^\mathrm{T}, \tag{4}$$

where k represents the kth ensemble member, and N is the ensemble size.

Sampling errors due to limited ensemble size will cause unreliable background error correlations between analysis points and observations at large distance. In our study, we settle this problem by using a Schur product (Houtekamer and Mitchell, 2001), which is often called "covariance localization". In Eq.

(3), ρ^o donates a Schur product of a quasi-Gaussian correlation matrix with the background error covariance matrix, and the correlation function ρ is defined as a fifth-order piecewise rational function proposed by Gaspari and Cohn (1999) as follows,

$$\rho(r,c) = \begin{cases} -\frac{1}{4}(r/c)^5 + \frac{1}{2}(r/c)^4 + \frac{5}{8}(r/c)^3 \\ \quad -\frac{5}{3}(r/c)^2 + 1, \qquad 0 \leqslant r \leqslant c; \\ \frac{1}{12}(r/c)^5 - \frac{1}{2}(r/c)^4 + \frac{5}{8}(r/c)^3 \\ \quad +\frac{5}{3}(r/c)^2 - 5(r/c) \\ \quad +4 - \frac{2}{3}(r/c)^{-1}, \qquad c \leqslant r \leqslant 2c; \\ 0, \qquad\qquad\qquad 2c \leqslant r, \end{cases} \tag{5}$$

where c is a pre-specified critical distance, and r is the distance between observations and analysis grid points:

$$r = \sqrt{r_x^2 + r_y^2 + r_z^2}. \tag{6}$$

In the EnSRF algorithm, observations are assimilated one at a time, $\boldsymbol{H}\boldsymbol{P}^\mathrm{f}\boldsymbol{H}^\mathrm{T}$ and $\boldsymbol{R}$ become scalars for one observation, and thus the calculation of $(\boldsymbol{H}\boldsymbol{P}^\mathrm{f}\boldsymbol{H}^\mathrm{T} + \boldsymbol{R})^{-1}$ becomes a scalar inversion. The implementation of sequential assimilation of observations and covariance localization settles the problem of huge computational costs in matrix inversion when calculating $\boldsymbol{K}$, which makes the EnKF algorithm feasible for large systems.

The deviation of kth ensemble member from the mean is updated by:

$$x_k'^\mathrm{a} = \gamma(I - \widetilde{\boldsymbol{K}}\boldsymbol{H}(x_k'^\mathrm{f}))x_k'^\mathrm{f}, \tag{7}$$

where

$$\widetilde{\boldsymbol{K}} = \boldsymbol{K}\left(1 + \sqrt{\frac{\boldsymbol{R}}{\boldsymbol{H}\boldsymbol{P}^\mathrm{f}\boldsymbol{H}^\mathrm{T} + \boldsymbol{R}}}\right)^{-1}, \tag{8}$$

and γ is a covariance inflation factor, which is used to adjust the spread of ensemble, thus relieving the filter divergence caused by sampling errors in the estimation of $\boldsymbol{P}^\mathrm{f}$ due to small ensemble sizes. Ensemble variance should represent the statistics of the error of the ensemble mean forecast. Small ensemble spread tends to

make the analysis algorithm reject observations; otherwise, the analysis algorithm rejects background. In practice, the deviation of each member from the ensemble mean is multiplied by this inflation factor before the first observation is assimilated.

Both radial velocity and reflectivity are assimilated in this study. The observation operator for radial velocity and reflectivity are the same as that in Tong and Xue (2005). V_r is calculated from

$$V_r = u \cos\alpha \sin\beta + v \cos\alpha \cos\beta + w \sin\alpha, \qquad (9)$$

where V_r is the observation of radar radial velocity, α and β are elevation angle and azimuth angle of radar beams respectively, and u, v, and w are the three wind components output from the WRF model.

The observation operator for reflectivity is:

$$Z = 10 \lg Z_e, \qquad (10)$$

where Z_e is reflectivity factor in unit of $\mathrm{mm}^6\ \mathrm{m}^{-3}$, and Z is its logarithm in unit of dBZ. Z_e is estimated as the sum of contributions from three categories of hydrometeors: reflectivity from rain Z_{er}, snow Z_{es}, and hail Z_{eh}, i.e.,

$$Z_e = Z_{er} + Z_{es} + Z_{eh}. \qquad (11)$$

The computation of each component of reflectivity is based on Smith et al. (1975) and Lin et al. (1983) as follows. Reflectivity for rain is

$$Z_{er} = \frac{10^{18} \times 720(\rho q_r)^{1.75}}{\pi^{1.75} N_r^{0.75} \rho_r^{1.75}}, \qquad (12)$$

reflectivity for dry snow when temperature is below 0°C is

$$Z_{es} = \frac{10^{18} \times 720 K_i^2 \times \rho_s^{0.25}(\rho q_s)^{1.75}}{\pi^{1.75} K_r^2 N_r^{0.75} \rho_i^2}, \qquad (13)$$

while reflectivity for wet snow when temperature is above 0°C is

$$Z_{es} = \frac{10^{18} \times 720(\rho q_s)^{1.75}}{\pi^{1.75} N_s^{0.75} \rho_s^{1.75}}, \qquad (14)$$

and reflectivity for hail is

$$Z_{eh} = \left(\frac{10^{18} \times 720}{\pi^{1.75} N_h^{0.75} \rho_h^{1.75}} \right)^{0.95} (\rho q_h)^{1.6625}, \qquad (15)$$

where ρ is air density, specifically, $\rho_r = 1000\ \mathrm{kg}\ \mathrm{m}^{-3}$ is the density of rainwater, $\rho_s = 917\ \mathrm{kg}\ \mathrm{m}^{-3}$ is the density of snow, $\rho_i = 913\ \mathrm{kg}\ \mathrm{m}^{-3}$ is the density of ice, and $\rho_h = 913\ \mathrm{kg}\ \mathrm{m}^{-3}$ is the density of hail; q_r, q_s, and q_h are the mixing ratios for rain, snow, and hail, respectively; $N_r = 8.0 \times 10^{-6}\ \mathrm{m}^{-4}$, $N_s = 3.0 \times 10^{-6}\ \mathrm{m}^{-4}$, and $N_h = 4.0 \times 10^{-6}\ \mathrm{m}^{-4}$, which are the intercept parameters in the assumed Marshall-Palmer exponential drop size distributions for rain, snow, and hail respectively. $K_i^2 = 0.176$ and $K_r^2 = 0.93$ are the dielectric factors for ice and water, respectively.

The feasibility of this assimilation system has been tested by Qin et al. (2012) through OSSEs. In this study, the effect of assimilating real radar data is explored by applying the assimilation system to a squall line case study.

3. Description of the case

3.1 Overview of the event

A squall line hit midwest Shandong Province on 12 July 2005 under the synoptic environment of a transverse (east-west oriented) trough related to a northeast vortex being transformed into a north-south oriented trough. From 1100 to 1500 BT (Beijing Time), thunder storm, strong winds, and hail occurred in succession at Gaotang, Yucheng, Qihe, Jinan, Laiwu, Boshan, and Yiyuan stations of Shandong Province, and hail occurred mainly at Gaotang, Yucheng, Laiwu, and Yiyuan stations. The diameter of hail observed at Xinzhuang town of Laiwu city was about 25 mm, and the maximum accumulated hail reached 30–40 mm. Strong wind was observed in the region between Jinan and Yiyuan stations, with wind speed above 20 m s^{-1}. Instantaneous wind speed reached 22.4 m s^{-1} at Laiwu station at 1330 BT, and 29.2 m s^{-1} at Yiyuan station at 1440 BT. This squall line has caused enormous economic loss in Shandong Province.

3.2 Synoptic environment of the event

A vortex stayed over Northeast China from 8 to 11 July, behind which a ridge strengthened and developed northeastward. The vortex center then weakened and moved southward, with a transverse trough

generated to its west. At 0800 BT 12 July, the vortex disappeared, accompanied with an anticlockwise turning of the transverse trough. The prevailing wind direction at 500 (Fig. 1a) and 700 hPa (figure omitted) was west-northwest over Shandong Province. At 850 hPa (Fig. 1b) and below, a cyclonic shear lay over the boarder of Hebei, Henan, and Shandong provinces, and the wind in midwest Shandong Province was weak southwesterly. The sounding at Zhangqiu station revealed that the 24-h temperature tendency at 0800 BT 12 July was +2℃ at 850 hPa and –1℃ at 500 and 700 hPa. This indicated that temperature increased obviously in the low troposphere, while cold air invaded the mid-upper troposphere. In such a synoptic environment of the transverse trough being transformed into a north-south one, the upper-level cold air went down and unstable stratification formed, inducing severe convective weather.

3.3 Precipitation process

The squall line system moved from west to east in midwest Shandong Province, and precipitation developed along with it. Thunder shower less than 1 mm occurred at 0800 BT 12 July in Northwest Shandong. The intensity and range of precipitation increased from 1200 to 1700 BT, and local precipitation increased obviously. Rainfall intensity was 18 mm h^{-1} at 1200 BT, and reached its maximum value of 43 mm h^{-1} at 1400 BT around Tai'an station, then weakened to be 12 mm h^{-1} at 1600 BT around Yiyuan station. The precipitation abated to a general thunder shower

at 1800 BT, and located mainly in the area of high surface pressure. From 1800 to 2000 BT, precipitation continued to abate and gradually moved out of Shandong Province.

3.4 Radar observations

This mesoscale convective event was observed by the CINRAD-SA Doppler radar in Qihe county of Jinan area (with radar antenna located at 36.81°N, 116.78°E, and 72.9 m above sea level). The volume scan mode of the radar was VCP 21, of which the radar completed 9 elevations ranging from 0.5° to 19.5° within 5–6 min. The radar gave observations of reflectivity and radial velocity at each elevation, with maximum detection radius of 460 and 230 km respectively, and resolutions of 250-m gate spacing and 1° azimuth respectively.

The evolution of composite reflectivity field showed that the convective storm was initiated in the early morning of 12 July near Yangquan city of Shanxi Province. It developed eastward, and then two convective cells formed at 1056 BT in Xiajin county of Dezhou area (with maximum reflectivity of 55 dBZ and echo top at 12 km) and Qinghe county of Hebei Province. They strengthened and evolved end to end gradually (Fig. 2a). An intense echo emerged near Gaotang station at 1126 BT (Fig. 2a) and developed southward, while a bow-shaped echo began to develop in the western portion of the echo with maximum reflectivity of 68 dBZ at 1202 BT. At the same time, a clear outflow boundary occurred behind the new born
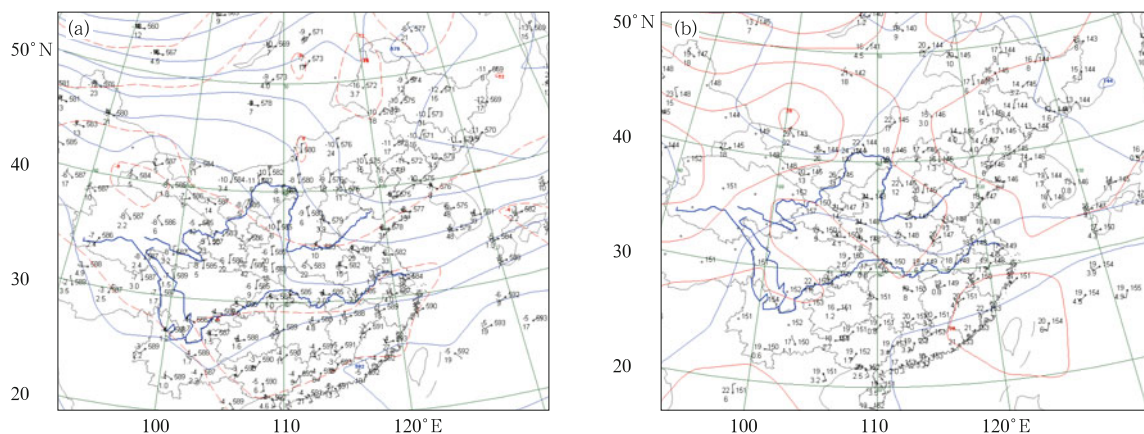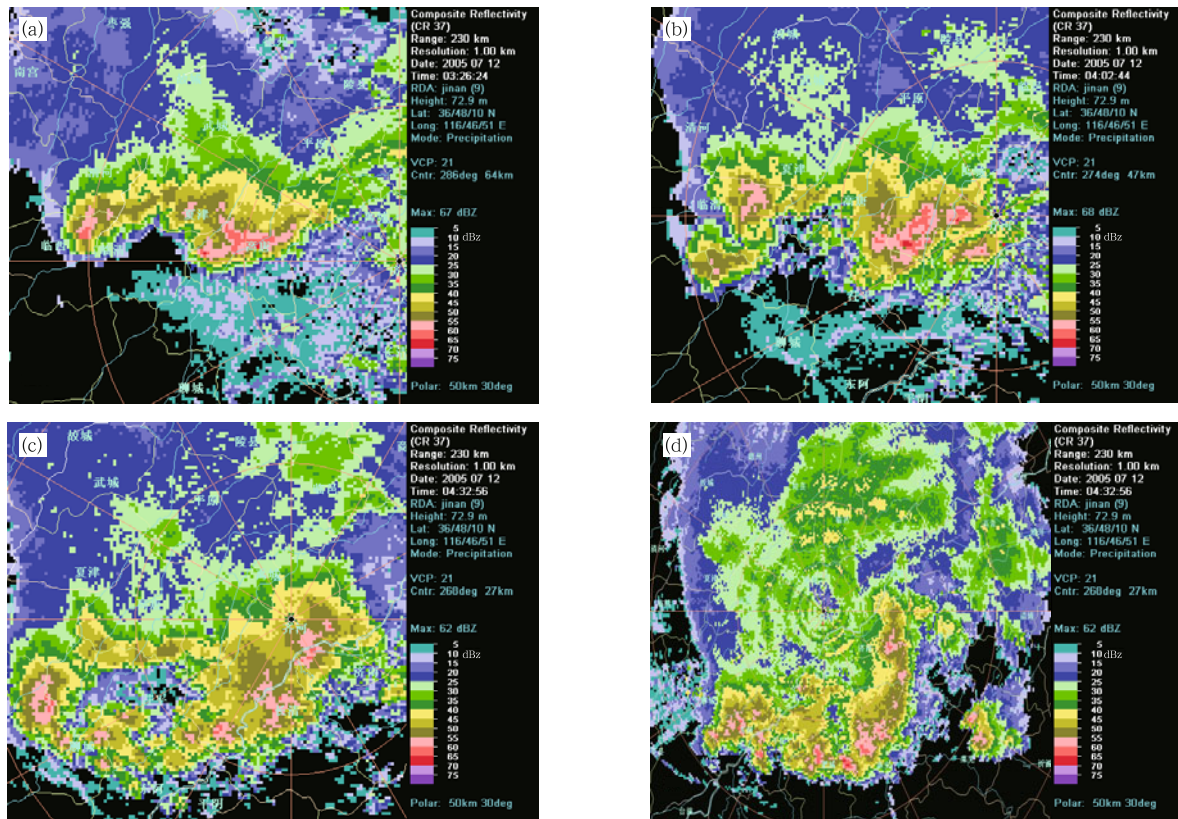

Fig. 1. Synoptic charts of (a) 500 and (b) 850 hPa at 0800 BT 12 July 2005.

Fig. 2. Compound radar reflectivity at Jinan at (a) 1126, (b) 1202, (c) 1232, and (d) 1321 BT 12 July 2005.

echoes, and convective cells formed continuously on the tail of it. The bow-shaped echo formed at 1232 BT (Fig. 2c) with convergence of the new-born convective echo and the former echo, and an echo notch appeared on the back side of the bow's head, indicating a strong inflow on the back side of the bow echo. During 1100–1300 BT, with the bow echo passing through, hail occurred in Gaotang and Yucheng, and thunderstorm gale occurred in Liaocheng and Jinan, with gust velocity of 18 m s^{-1}. The bow echo moved southward and converged with new-born cells, and began to weaken after 1357 BT. An isolated massive echo formed near Laiwu at 1238 BT, strengthened while moving northeastward, and reached maximum reflectivity of 63 dBZ at 1321 BT. It then began to weaken and dissipate at 1609 BT. At the same time, new convective cells developed on the right side of the aforementioned echo, and developed into a supercell at 1339 BT, with maximum reflectivity of 67 dBZ and echo top of 13 km. Affected by this supercell, hail and

thunderstorm gale hit Laiwu. The bow echo evolved into a comma cloud during 1403–1421 BT, and moved southeastward over Shandong Province from then on, and gradually dissipated.

4. Experimental design

4.1 Experiment scheme

This study includes two experiments as shown in Fig. 3: the assimilation experiment of real radar data and the control run without data assimilation. Both experiments begin at 0800 BT 12 July 2005, with integration time of 12 h that covers the whole development of the squall line event. The NCEP global reanalysis data are used as initial and boundary conditions. In the assimilation experiment, the model first integrates 1 h before the first assimilation at 0900 BT in order to develop a flow-dependent background error covariance that corresponds to the synoptic process. Then, real radar observations are assimilated every 30 min
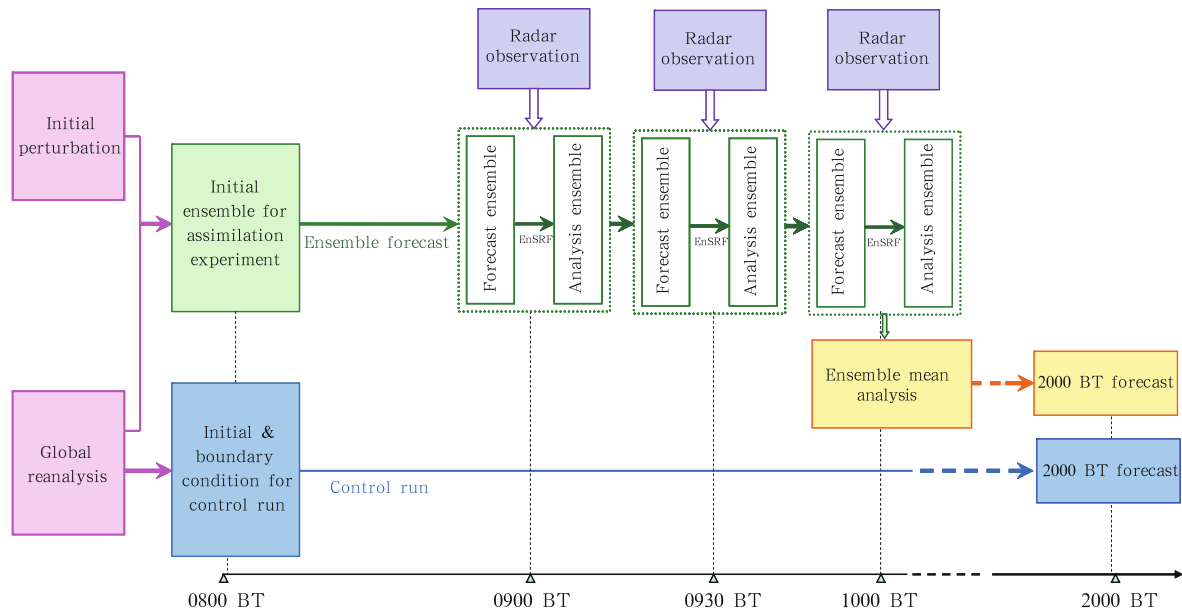
Fig. 3. Flow chart of the experiment scheme.

at 0930 and 1000 BT, and a deterministic forecast of 10 h is followed thereafter, initialized by the ensemble mean analysis of the 3rd assimilation cycle.

4.2 The forecast model

In this study, version 3.2 of WRF, a fully compressible nonhydrostatic mesoscale model, with its Advanced Research WRF dynamic core, is used. It has six prognostic equations and one static diagnostic equation. The prognostic variables include three velocity components, perturbation potential temperature, perturbation geopotential, and perturbation surface pressure of dry air, and optional prognostic variables such as mixing ratios for water vapor, cloud water, rain, ice, snow, and graupel. Two model domains with two-way nesting are employed. The coarse domain has 201×201 grid points and a grid space of 9 km, and the integration time step is 60 s. The inner domain has 280×247 grid points and a grid space of 3 km. Both model domains have 28 vertical layers, and the model top is set at 50 hPa. The cumulus parameterization scheme for coarse domain is the Kain-Fritsch scheme (Kain and Fritsch, 1990, 1993). No cumulus parameterization scheme is used in the inner domain. The microphysics scheme is WSM6 (WRF

Single-Moment 6-class) scheme (Hong et al., 2004) for both domains, from which mixing ratios of water vapor, cloud water, rain, ice, snow, and graupel can be output. The NCEP final FNL analysis data on a $1° \times 1°$ resolution are used to create the initial and boundary conditions.

4.3 Assimilation parameters

Both radar reflectivity and radial velocity are assimilated and all variables are updated in this study. Data assimilation is performed only for the inner domain. The cutoff radii of covariance localization are 10 model grids horizontally and 5 model grids vertically, and the covariance inflation factor is set to 2.0. Observation operators are given by Eqs. (9)–(15). Limited by computer resources, the ensemble size is set to 20. Encouraged by our previous results of OSSEs that model storm can be reasonably rebuilt after three assimilation cycles (Qin et al., 2012), three assimilation cycles are performed in this study.

4.4 Ensemble initial perturbations

The initial ensemble is generated by the WRF three-dimensional variational data assimilation (3DVAR) using the cv3 background error covariance option, same as Zhang et al. (2006) in which they used

3DVAR of the nonhydrostatic fifth-generation Pennsylvania State University-National Center for Atmospheric Research Mesoscale Model (MM5) to generate initial ensemble for their EnKF system. Firstly, 20 random perturbations of stream function, namely control vectors, which are consistent with the background error covariance used by the WRF 3DVAR system, are generated, and then transformed back to model space via a recursive filter in horizontal direction, an empirical orthogonal function (EOF) transform in vertical direction, and physical transformation. The initial perturbation is largely geostrophic balanced, which includes horizontal wind components, potential temperature, and mixing ratio for water vapor. Other prognostic variables such as vertical velocity and mixing ratios for cloud water, rain, ice, snow, and graupel are not perturbed.

5. Preprocessing of radar data

5.1 Quality control

Preprocessing and quality control of radar data are performed as follows:

(1) Ground clutter is identified and removed by analyzing the three-dimensional structure characteristics of radar reflectivity. Ground clutter rejection is implemented by means of calculating horizontal texture of reflectivity, vertical gradient of intensity, and the restrictive value of vertical gradient, and then gaps in precipitation echo areas potentially created by the algorithm are filled by using the echo information (Xiao, 2007).

(2) Radar observations, radial velocity as well as reflectivity, are thinned to the resolution of 4 km in the radial direction, and the resolution after data thinning is almost the same as the model grid spacing.

(3) The observation errors of reflectivity and radial velocity are assumed to be 5 dBZ and 3 m s^{-1} respectively in this study. The observation will be discarded if the difference between observation and background is larger than three times of the observation error.

5.2 Observations to be assimilated

A significant amount of observations have been discarded after quality control and preprocessing (see Table 1). Reflectivity data to be assimilated account for about 2%–3% of one volume scan, and radial velocity data to be assimilated only account for about 1% of one volume scan. Corresponding to the time of 3 assimilation cycles at 0900, 0930, and 1000 BT, the Doppler radar volume scans used in the current study are at 0901, 0931, and 1001 BT. Figure 4 shows the observations to be assimilated in the first assimilation cycle after preprocessing, in which obser-
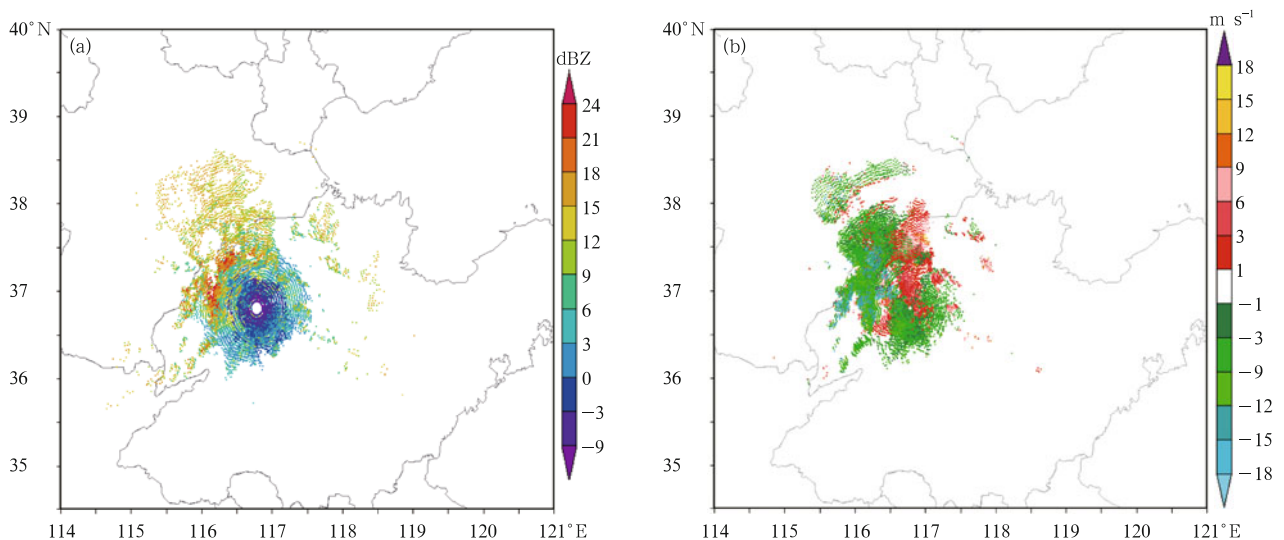
Fig. 4. Observations of (a) reflectivity (dBZ) and (b) radial velocity (m s^{-1}) to be assimilated in the first assimilation cycle.

Table 1. Number of radar observations to be assimilated

Time of radar volume scan	Number of Obs		Number of Obs assimilated		Percentage	
	Z	V_r	Z	V_r	Z	V_r
0901 BT	764898	2327173	22892	19965	2.99%	0.86%
0931 BT	764606	2326413	21194	19910	2.72%	0.86%
1001 BT	765659	2328374	16971	19016	2.22%	0.82%

vations of different heights are projected to a horizontal plane.

Table 1 shows the number of observations before and after data preprocessing used in the three assimilation cycles, and the percentage of observations to be assimilated in the volume scan.

6. Results

6.1 Performance of EnSRF

In this section, comparisons of wind fields, hydrometeor fields, and precipitation are made between forecasts of control run, ensemble mean forecasts, ensemble mean analyses of the assimilation experiment, and observations, so as to assess the performance of the EnSRF scheme in retrieving the dynamical and microphysical fields of the squall line case.

6.1.1 Wind fields

The performance of the EnSRF scheme in analyzing the low-level horizontal wind field is assessed by comparisons between radial velocity observations in plane position indicator (PPI) at 0.5° elevation and wind fields of control run and assimilation experiment. During 0900–1000 BT 12 July, radial velocity northwest of the Jinan radar is departing from radar with a maximum value of 19 m s^{-1}, and radial velocity southeast and south of the radar is orientating toward radar and is 5–10 m s^{-1}. Thus, at low levels below 850 hPa,

strong southeast wind prevails northwest of the radar in Qinghe, Xiajing, Linqing, and Wucheng areas, and weak southwest wind occurs southwest of the radar in Yanggu area. Weak south wind occurs south of the radar near Dongping county, and over the boarder of Shandong and Hebei provinces there is a cyclonic wind shear from southwest to southeast.

Radial velocity of ensemble mean analyses of the three assimilation cycles can be calculated from the observation operator for radial velocity (Eq. (9)), and the distribution of thus calculated radial velocity on the fifth model level (about 900 hPa) are shown in Fig. 6. It is seen by comparing Fig. 5 with Fig. 6 that radial velocity fields at 900 hPa from the ensemble mean analysis are basically in accordance with the observations.

Figure 7 shows the horizontal wind vector at 900 hPa from the control run, ensemble mean forecast, and ensemble mean analysis at 0930 BT 12 July 2005. Equivalent figures at 0900 and 1000 BT are omitted. It can be seen that, in the west and central parts of Shandong Province, the wind fields at 900 hPa of the control run are smooth, weak, and southward, which are inconsistent with the observations characterized by strong southeast wind and a cyclonic shear at low levels in the northwest of Shandong. In contrast, the radial velocity fields from the ensemble mean analysis are in good accordance with the observations, and
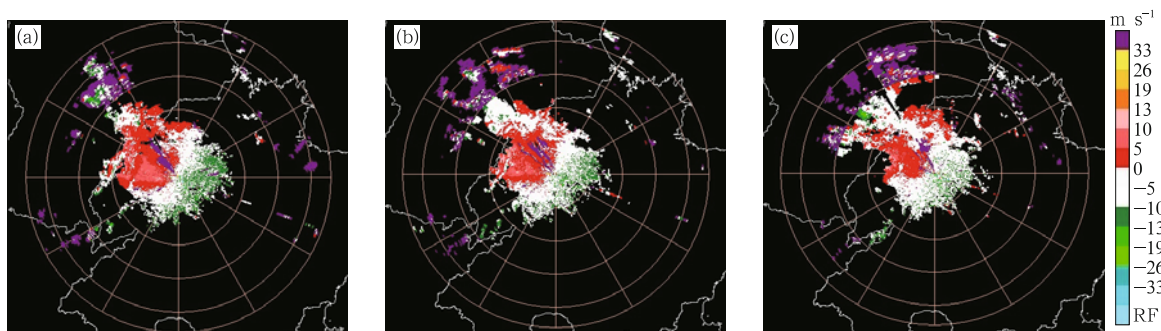
Fig. 5. Radial velocity PPI observations at 0.5° elevation at (a) 0901, (b) 0931, and (c) 1001 BT 12 July 2005.
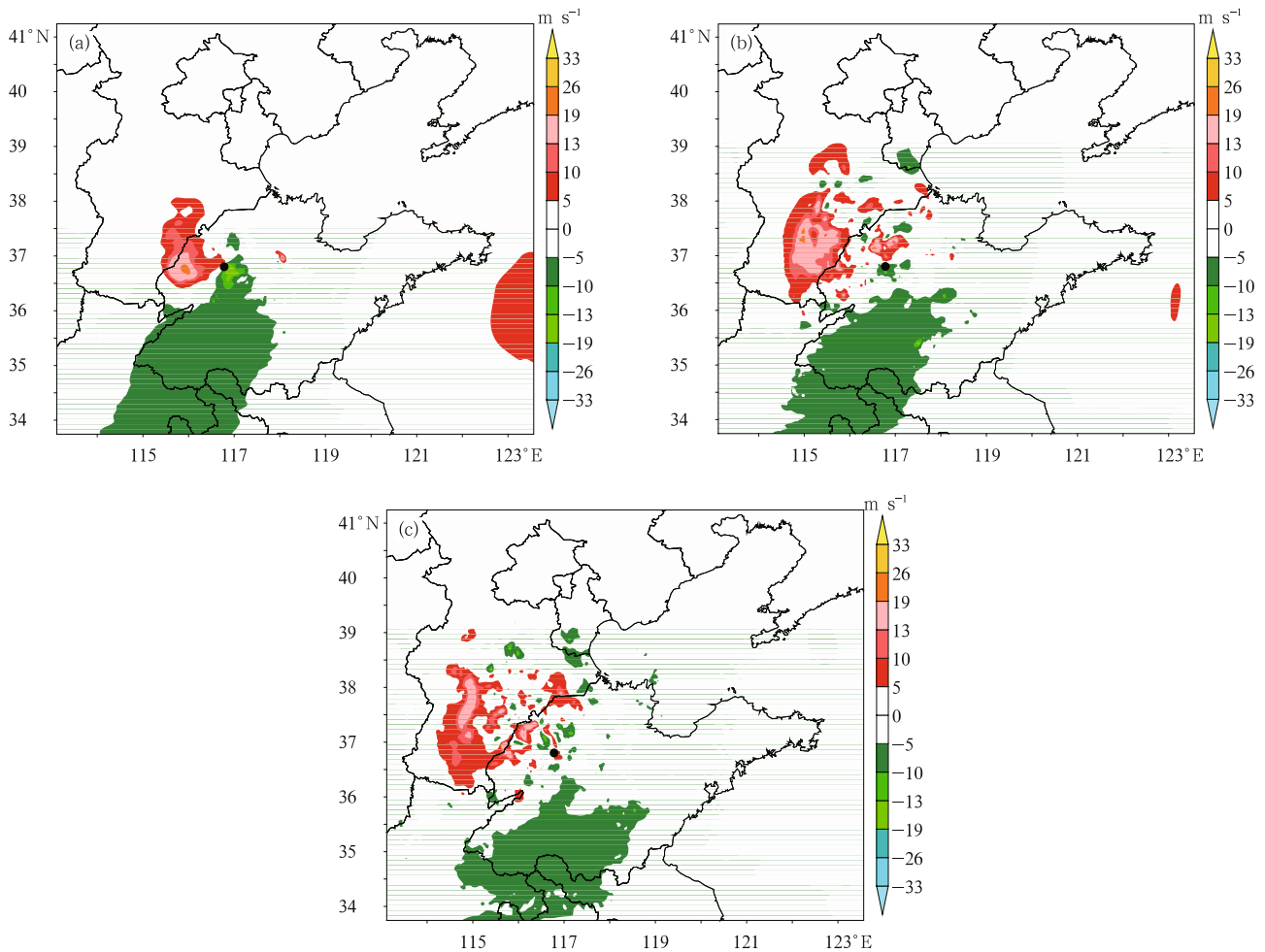
Fig. 6. Radial velocity at about 900 hPa calculated from the ensemble mean analysis at (a) 0900, (b) 0930, (c) 1000 BT 12 July 2005. The black dot denotes location of the Jinan radar.

radial velocity greater than 19 m s^{-1} departing from the radar can be seen around Qinghe, Xiajing, and Linqing areas in Fig. 6. An obvious wind shear extending from south-southwest to southeast over the boarder of Shandong and Hebei provinces is seen in the ensemble mean forecast and ensemble mean analysis at 900 hPa, which is consistent with the low-level observations. Moreover, after data assimilation, the south wind around Lingxian becomes stronger, and agrees better with observations. The low-level wind shear, strengthening southeast wind around Qinghe, Xiajing, and Linqing, together with strengthening south wind around Lingxian, cause a low-level wind convergence in Northwest Shandong, which all contribute to the generating of updraft by the model atmosphere, and

this has made preparations for the advent of the subsequent convective weather.

Through comparison between radial velocity calculated from control run and assimilation experiment, and radial velocity observations at 1.5° and 2.4° elevations, the analyzed upper-level wind fields after assimilation are closer to the observations than that of the control run. From radial velocity PPI observations at 1.5° and 2.4° elevations at 0901, 0931, and 1001 BT, it can be seen that at 500 hPa, a strong northwest air flow appears in the northwest of Shandong Province and south of Hebei Province, and a weak west southwest air flow shows up in the central and southwest of Shandong Province, and there is a trough oriented from northwest to southwest in the upper air above
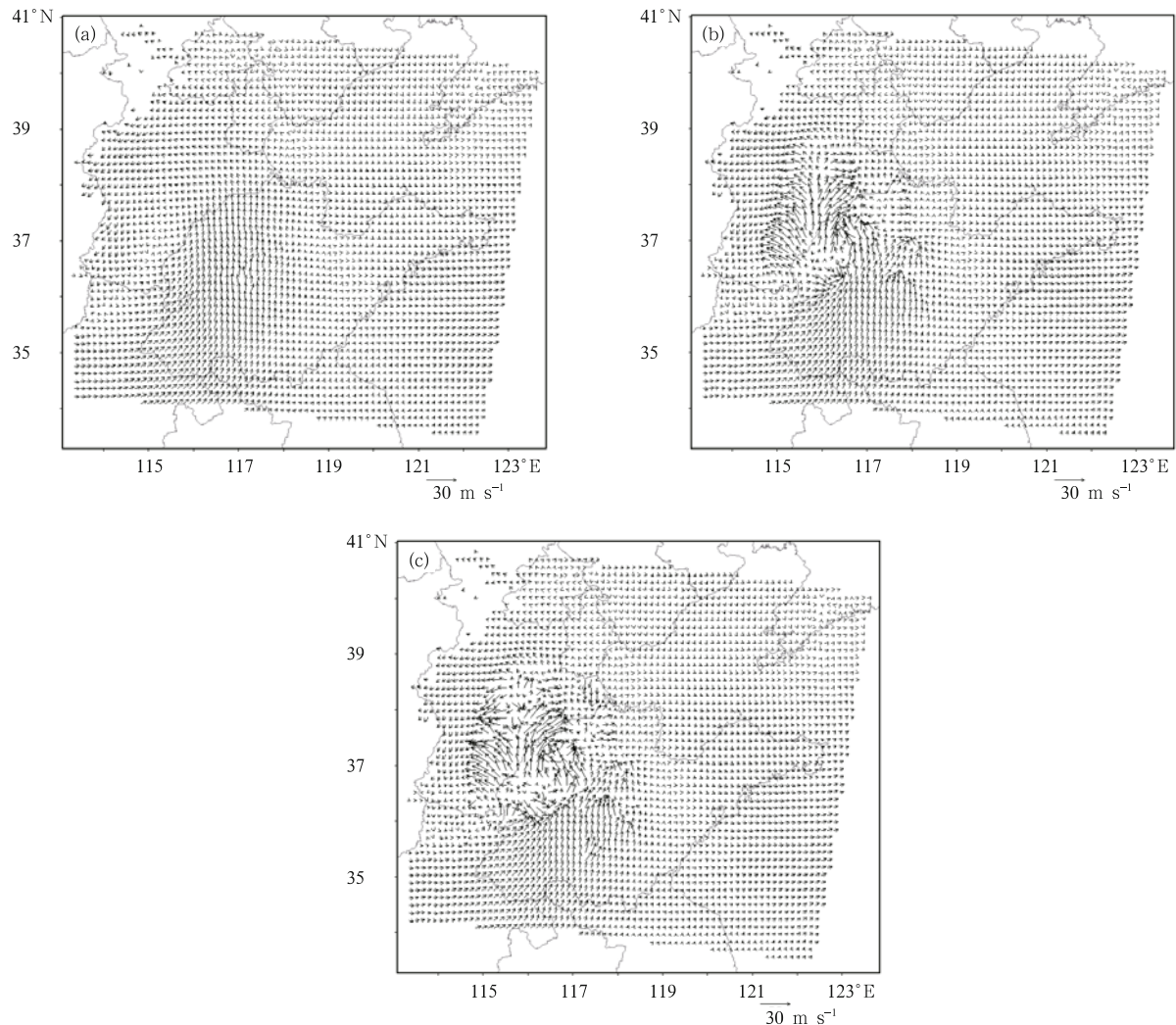
Fig. 7. Horizontal wind vector at 900 hPa from (a) control run forecast, (b) ensemble mean forecast, and (c) ensemble mean analysis, of the second assimilation cycle at 0930 BT 12 July 2005.

the radar. In comparison with the radial velocity calculated from ensemble mean analysis of the 10th model level (about 550 hPa), it is found that, after assimilation, the radial velocity in upper air is in good accordance with the observation, with radial velocity of 19 m s^{-1} orientating toward radar in the northwest and southwest of the radar, and radial velocity departing from radar in the east of the radar.

A comparison of horizontal wind fields at 500 hPa at 0900, 0930, and 1000 BT from the control run, ensemble mean forecast, and ensemble mean analysis shows that although the control run produces the trough at 500 hPa, the flow field is too smooth to de-

scribe the strong northwest air flow along the Dezhou, Hengshui, Xinji, and Wuji areas; while the northwest air flow is strengthened in the aforementioned area after assimilation, and the wind fields in Hejian and Xianxian of Hebei Province have also been better simulated.

We now examine the performance of the EnSRF in retrieving the vertical wind field. As analyzed above, the low-level horizontal wind fields converge around 37.2°N during 0900–1000 BT, and there occur vigorous convective clouds and strong vertical motion there. A cross-section of velocity, temperature, and total mixing ratio of hydrometeors (sum of mix-

ing ratio for cloud water, rain, ice, snow, and graupel) along 37.2°N is plotted for the control run forecast, ensemble mean forecast, and ensemble mean analysis at 0900, 0930, and 1000 BT. It can be seen that, the increase of vertical velocity from the control run is slow and weak and does not reach 1 m s^{-1} until 1000 BT, and the total mixing ratio of hydrometeors from the control run is also very small (Fig. 8b). Such weak vertical motion and low content of hydrometeors do not accord with observation of the severe convective system. By contrast, in the assimilation experiment, the upward velocity before the 1st assimilation cycle does not reach 0.5 m s^{-1} (Fig. 8c), but it increases obviously to 4 m s^{-1} after the 1st assimilation cycle

(Fig. 8d). Hydrometeors develop quickly along with the upward motion through model dynamics, and have a good correspondence in position with the upward flow. Vertical motion weakens at 1000 BT compared with that at 0930 BT, which is also in agreement with the observation that the convective clouds are weakening during this period.

As can be seen from the above, by assimilation of radar data using EnSRF, detailed characteristics of wind fields, such as cyclonic shear at the low level, the high velocity region, and low-level wind convergence in Xiajing area have been accurately retrieved. Moreover, the vertical motion has also been strengthened, which helps development of the convection. The
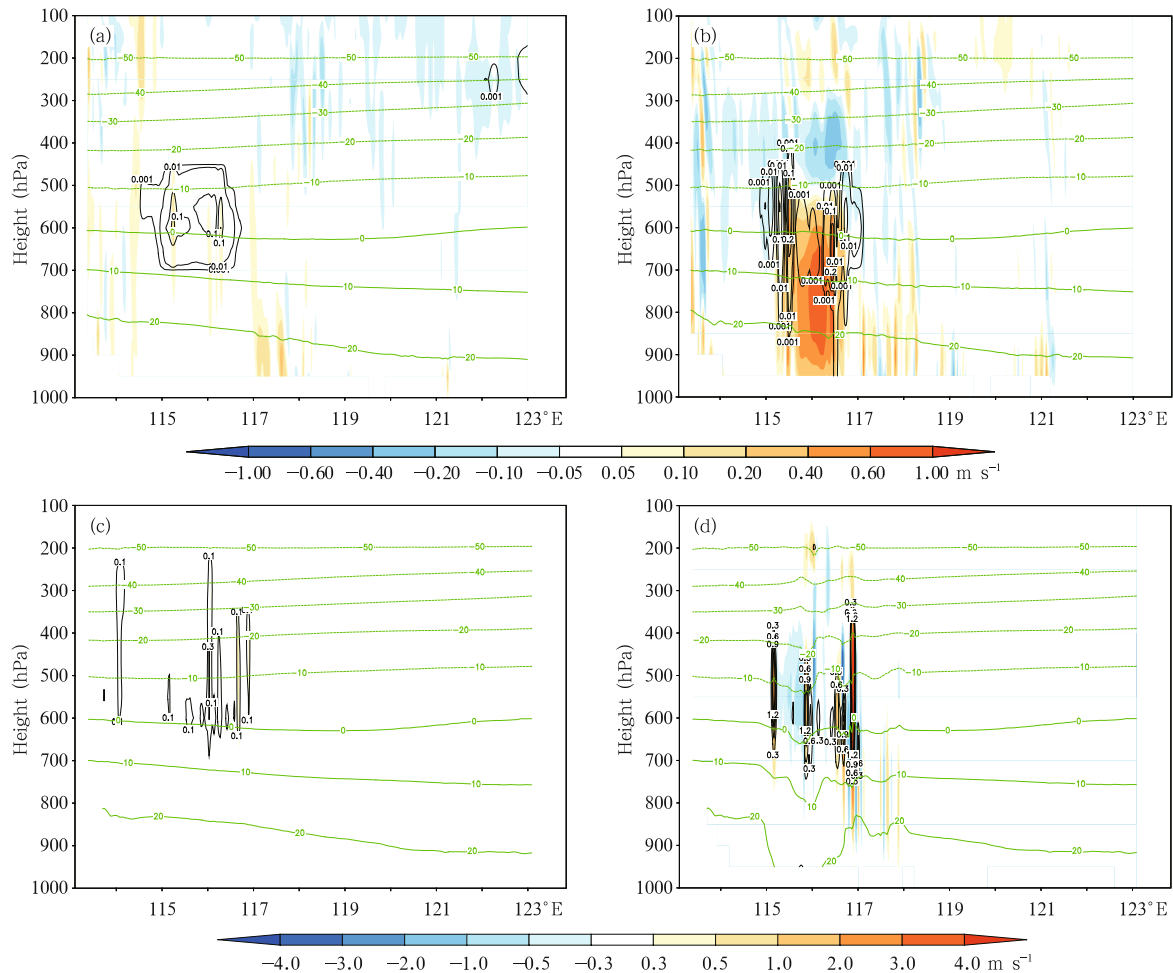
Fig. 8. Longitude-height cross-sections of vertical velocity (shaded), temperature (green contour), and total mixing ratio of hydrometeors (black contour; g kg^{-1}) along 37.2°N of (a) forecast of control run at 0900 BT, (b) forecast of control run at 1000 BT, (c) ensemble mean forecast at 0900 BT, and (d) ensemble mean analysis of the second assimilation cycle at 0900 BT 12 July 2005.

wind fields after assimilation of radar data agree better with the observations.

6.1.2   Microphysical fields

It can be seen from reflectivity PPI observations at 0.5° (Fig. 9) and 1.5° elevations (figure omitted) that convective cells develop northwest of the radar with maximum reflectivity of 60 dBZ, and weaken gradually from 0900 to 1000 BT. The height of this echo is about 2–5.5 km estimated from radial distance and elevation of the echo. There should be a region of high hydrometeor content between 700 and 500 hPa

accordingly. In the control run, the convection has not developed yet due to model spin-up. Hydrometeors only appear in local areas with a small value of less than 1.0 g kg^{-1} at 500 and 700 hPa (Figs. 10a$_1$–c$_1$ for 500 hPa; the 700-hPa figure is omitted). By contrast, in the assimilation experiment, information of hydrometeors is added into the analyzed field, and hydrometeor field has been greatly improved. The total mixing ratio of hydrometeors exceeds 1.0 g kg^{-1} in most areas, and in better accordance with the observations in the northwest of Shandong at 500 and
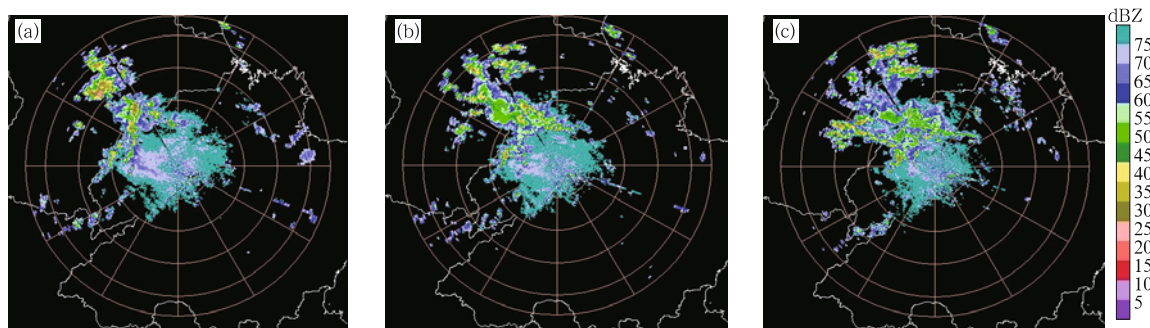
Fig. 9. Reflectivity PPI observations at 0.5° elevation at (a) 0901, (b) 0931, and (c) 1001 BT 12 July 2005.
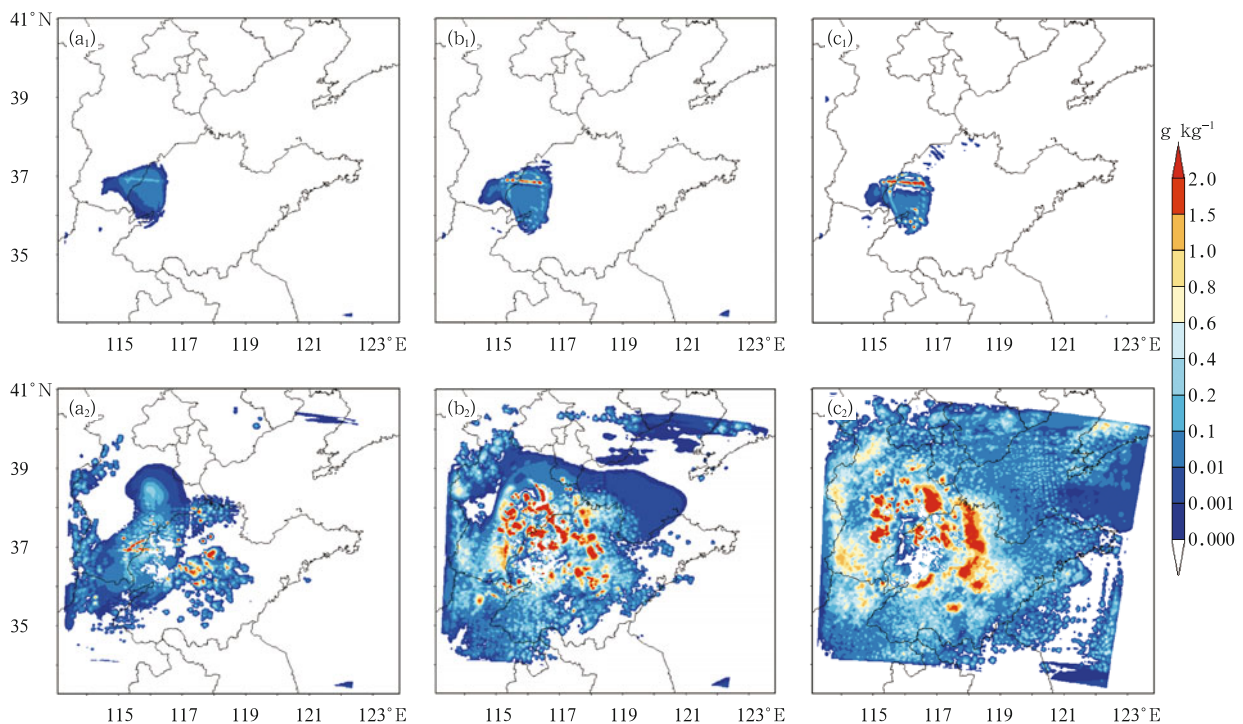
Fig. 10. Forecast total mixing ratio of hydrometeors (g kg^{-1}) at 500 hPa from the control run at (a$_1$) 0900, (b$_1$) 0930, and (c$_1$) 1000 BT, and ensemble mean analysis at (a$_2$) 0900, (b$_2$) 0930, and (c$_2$) 1000 BT 12 July 2005.

700 hPa (Figs. 10a$_2$–c$_2$).

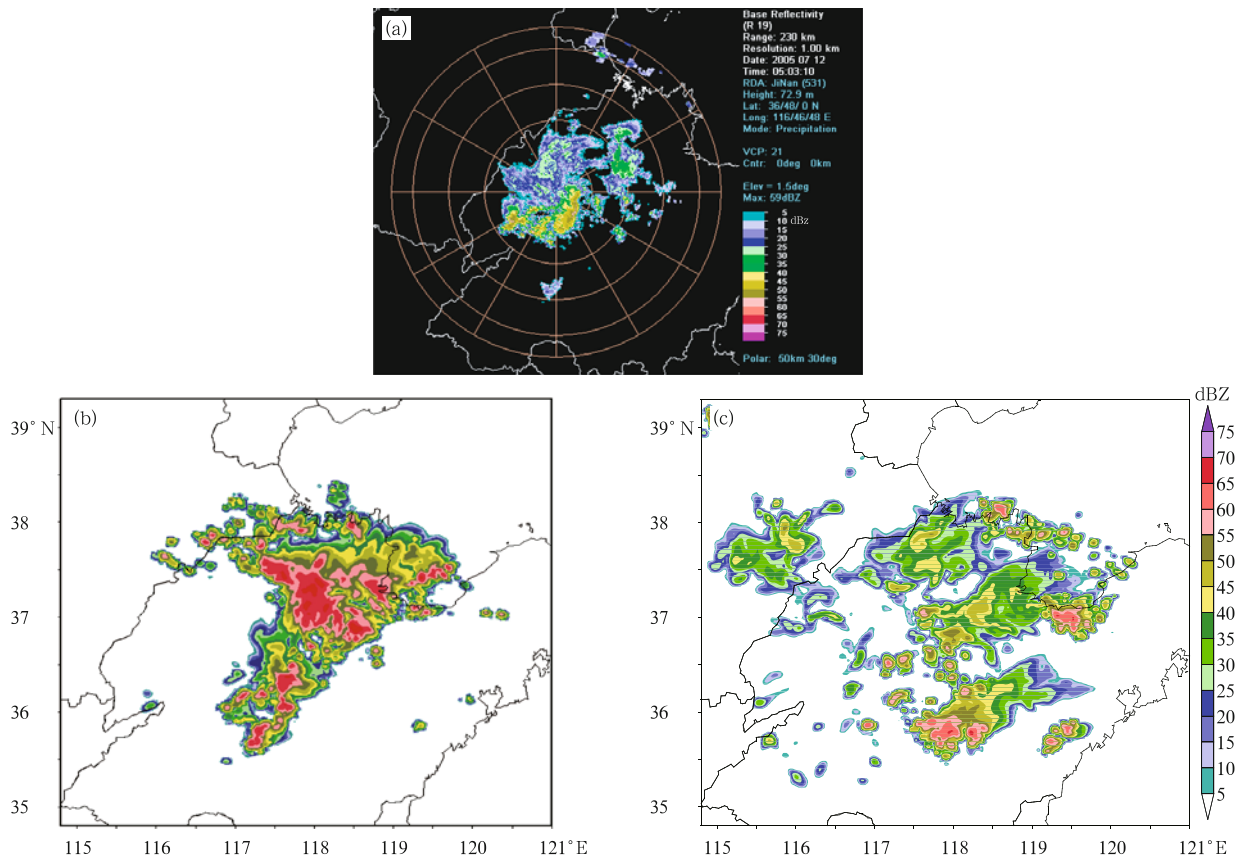## 6.2 Forecast from ensemble mean analysis

Encouraged by accurate retrieval of dynamic and thermal fields of the squall line with the use of the assimilation scheme, a deterministic forecast to 2000 BT is made from the ensemble mean analysis of the 3rd assimilation cycle. In this section, this forecast is assessed through comparison with the forecast from the control run and the observations.

6.2.1 Microphysical fields

Forecasts of microphysical fields from ensemble mean analysis will be verified by a comparison between forecast reflectivity and observed reflectivity. As shown in Fig. 11a, a bow-shaped echo lies south of Jinan at 1.5° elevation, with a radial distance of about 150 km from the radar and maximum reflectivity of 50 dBZ. It is estimated that the height of the echo is

4 km (600 hPa or so). The forecast reflectivity by the control run is much larger than the observation in a whole, with maximum values of basically 55–60 dBZ (Fig. 11b); while the forecast reflectivity by ensemble mean analysis has a closer distribution to the observation in the location of strong and weak echoes, and the value of reflectivity is also closer to the observation (Fig. 11c). Comparison of forecast reflectivity fields from both the control run and the assimilation experiment at 1400 BT with the observations shows that the forecast from ensemble mean analysis still has encouraging effects after a 4-h integration (figures omitted).

The forecast accuracy of ensemble mean analysis gradually decreases after model integration for 5 h, as indicated by faster development and quicker movement of the simulated squall line than the observed. This may be attributed to a relatively stronger west wind that is assimilated into the model. But the fore-

Fig. 11. (a) Reflectivity PPI observation at 1.5° elevation at 1303 BT. Forecast reflectivity (dBZ) at 600 hPa from (b) control run and (c) ensemble mean analysis of the assimilation experiment at 1300 BT 12 July 2005.

cast from ensemble mean analysis is still closer to observation than that from the control run. After integration of 8 h, neither the forecast from ensemble mean analysis nor the forecast from the control run is in agreement with the observation.

Figure 12 shows the reflectivity PPI observation at 1.5° elevation at 1409 BT, and its vertical cross-section along line AB, located at about 35.7°N, and Fig. 13 is the vertical cross-sections of forecast reflectivity along 35.7°N from both the control run and the ensemble mean analysis. Figures 12 and 13 reveal that the squall line is well organized into a belt-shaped system and the forecast initiated from ensemble mean

analysis has a better performance in describing such a belt-shaped arrangement of convective cells, as well as in forecasting the height and intensity of each convective cell.

As shown by the visible cloud imagery from the Moderate Resolution Imaging Spectroradiometer (MODIS) at 1050 BT 12 July (Fig. 14), a small-scale but deep cloud system developed in the west of Shandong Province, with a shallow cloud periphery. The total hydrometeor at 500 hPa produced by the control run (Fig. 15a) is much less than the MODIS data, while the forecast hydrometeor field from the assimilation experiment (Fig. 15b) has a more reasonable
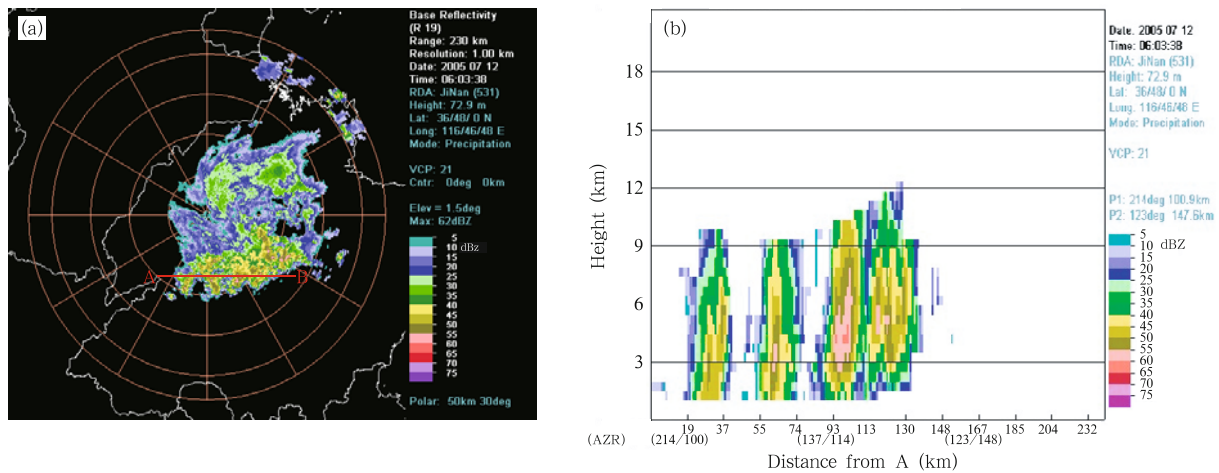
Fig. 12. (a) Reflectivity PPI observation at 1.5° elevation and (b) cross-section of reflectivity along line AB at 1409 BT 12 July 2005.
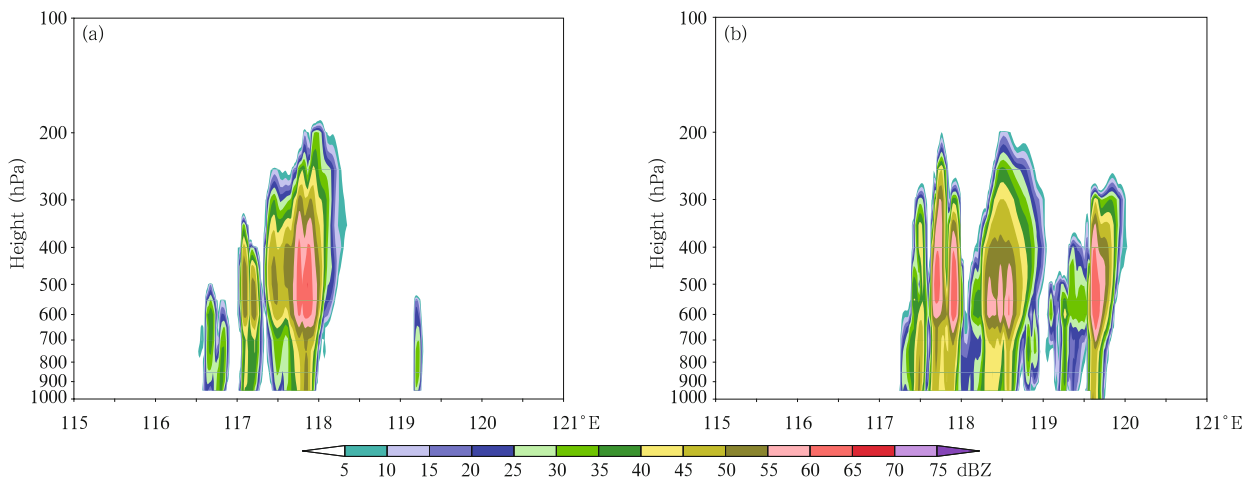
Fig. 13. Longitude-height cross-section of forecast reflectivity (dBZ) along 35.7°N from (a) control run and (b) ensemble mean analysis of the assimilation experiment at 1400 BT 12 July 2005.
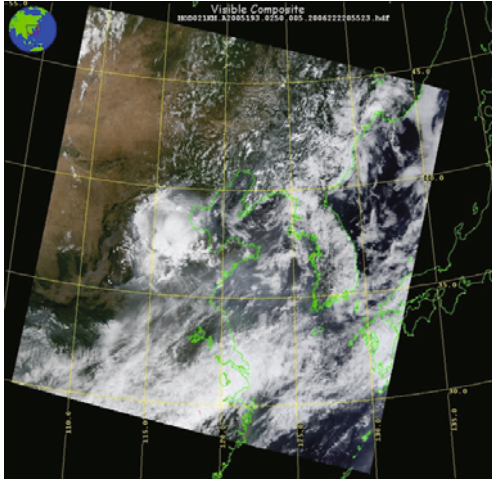
**Fig. 14.** Visible cloud imagery by MODIS at 1050 BT 12 July 2005.

distribution and structure.

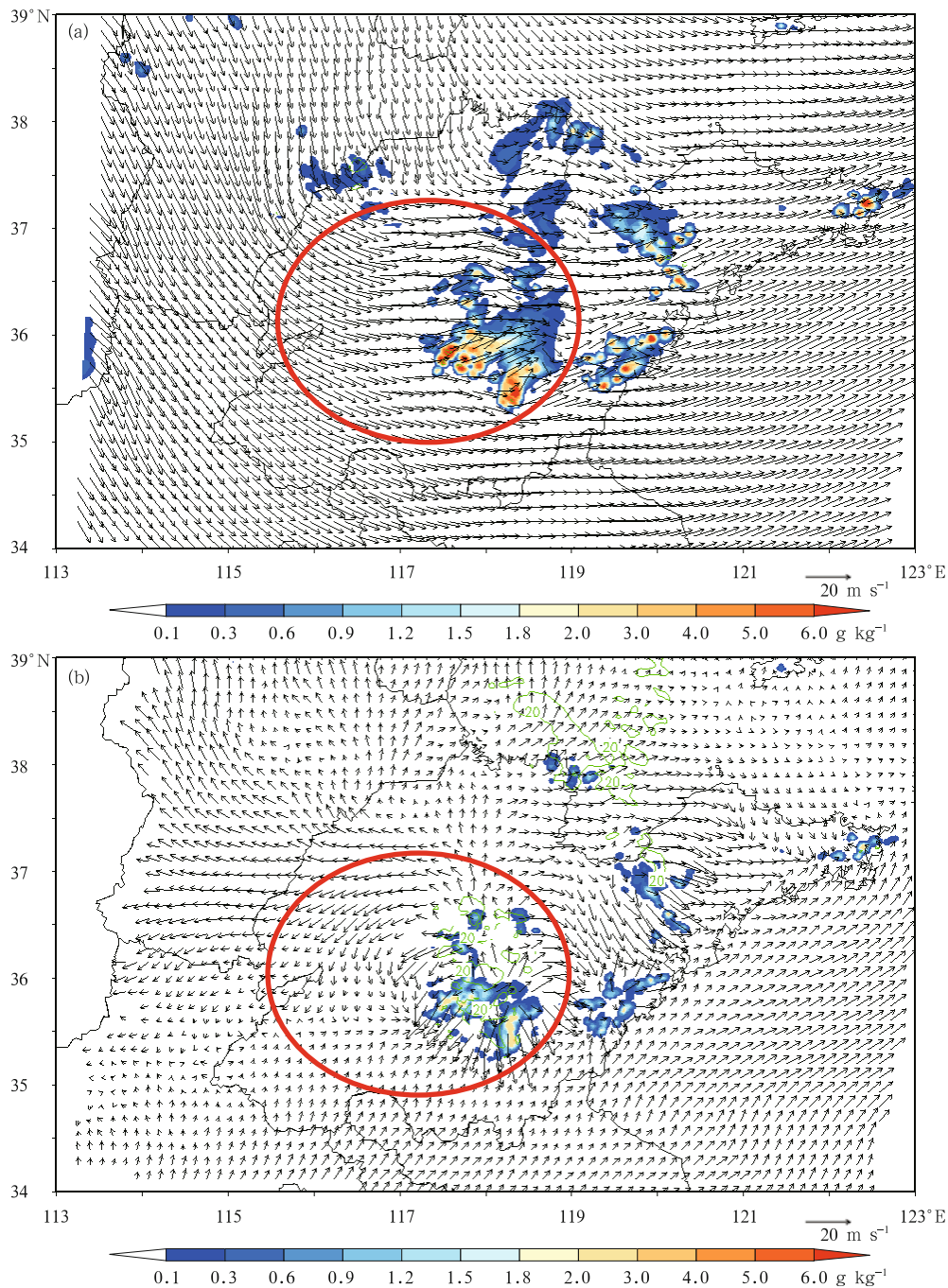### 6.2.2 Wind field and storm structure

Figure 16 shows the horizontal wind field and total mixing ratio of hydrometeors at 500 and 950 hPa after 4-h integration initiated from ensemble mean analysis of the 3rd assimilation cycle. An obvious vertical wind shear appears, as indicated by red circles in Fig. 16. The environment wind is mainly northwesterly and westerly above 850 hPa, and turns into east and south wind below 850 hPa. The shift of wind direction from the upper to the lower atmosphere can reach 90°–180°. Such a vertical wind shear conforms to the typical feature of the wind field and structure of a convective storm, and is favorable for maintenance and development of the storm (Yu et al., 2006).

As shown in Fig. 16b, at the leading edge of the storm, there is an outflow region for downdraft, where the horizontal wind speed reaches 20 m s^{-1}. During the saturation-adiabatic subsidence of rain droplets, the air is dragged down and cooled due to the evaporation and melting. The cold downdraft spreads outward near the ground layer and forms a cold outflow. It then converges strongly with the southwesterly warm moist air at the leading edge of the storm and forms a gust front, which is in accordance with the ground observations of gale and temperature decrease at 1400 BT. The strong convergence and unstable energy around the gust front drive continuous development of the storm. The vertical cross-section along 35.4°N of forecast total hydrometeor and temperature fields at 1400 BT shows that there is a cold pool in the convective cell near the boundary layer (figure omitted), which is caused by cold downdraft of precipitation particles, and there is a warm region in the middle of the convective cell, which might be caused by latent heat release of hydrometeors in that region, and corresponds to the dynamic and thermal characteristics of convective cells.
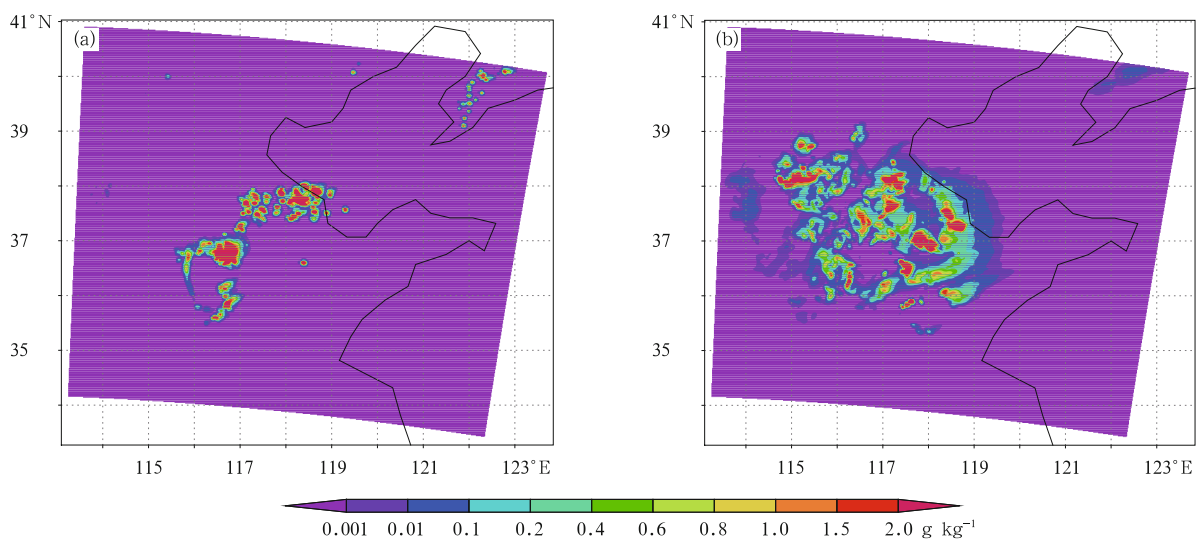
Fig. 15. Total mixing ratio of hydrometeors (g kg^{-1}) at 500 hPa from (a) control run and (b) ensemble mean analysis of the assimilation experiment at 1100 BT 12 July 2005.

Fig. 16. Horizontal wind field (vector) and total mixing ratio of hydrometeors (shaded; g kg^{-1}) by ensemble mean analysis at (a) 500 and (b) 950 hPa at 1400 BT 12 July 2005.

The above analysis has demonstrated that forecast of wind fields and storm structure initiated from ensemble mean analysis is consistent with the characters of convective cells, and the distribution and collocation of dynamic and thermal fields are also reasonable.
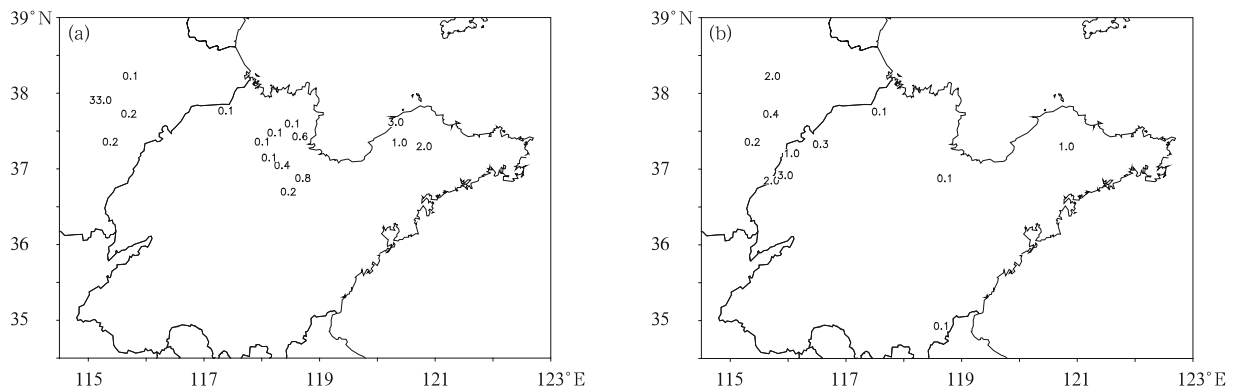
6.2.3 Precipitation

As shown by Fig. 17, precipitation occurred in southeast of Hebei, north of Shandong, and over the boarder of Hebei and Shandong provinces during

0800–0900 BT, with hourly rainfall exceeding 30 mm in some places. The control run starts at 0800 BT, and does not produce precipitation after 1.5-h integration at 0930 BT due to model spin-up (Fig. 18a). By contrast, precipitation occurs quickly after 0.5-h integration at 0930 BT, when the model is initiated from ensemble mean analysis of the 1st assimilation cycle at 0900 BT (Fig. 18b). Compared to the observation, precipitation forecast over the boarder of Hebei and Shandong during 0900–0930 BT by the assimilation experiment is basically correct. Although the amount of precipitation is a little bit larger, the precipitation area is in good consistency with the observation. By assimilation of radar data using EnSRF, the model spin-up time has been shortened and forecast of precipitation has been improved considerably.
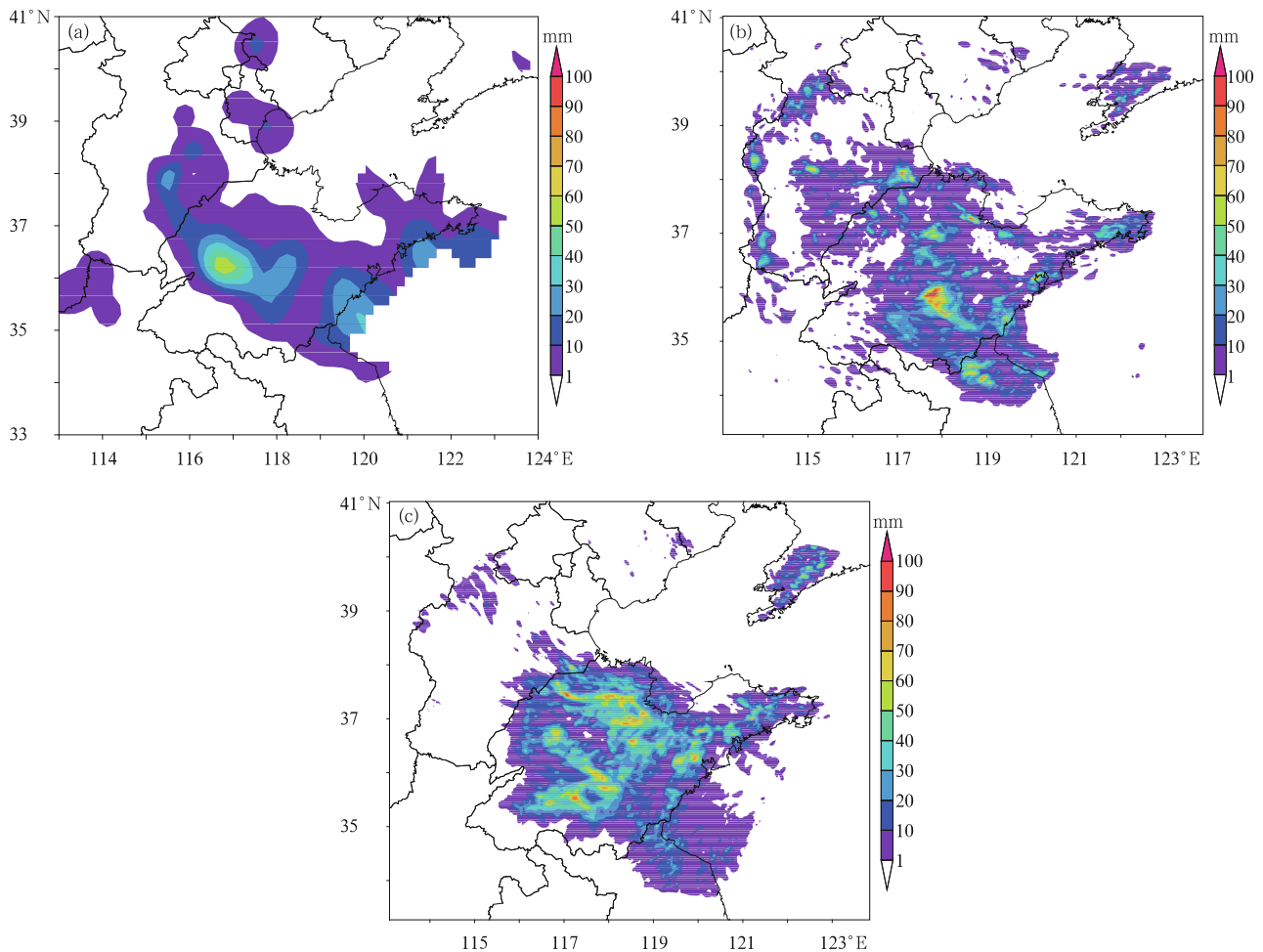
The accumulated precipitation observation in Fig. 19a indicates that the rain falls mainly in the midwest of Shandong Province, with a northwest-southeast belt-shaped distribution and a maximum value exceeding 60 mm at 36.3°N, 116.8°E. Precipitation forecast by the control run is larger than that of observation in general, especially in the north of Shandong (Fig. 19c). But it is greatly improved in the assimilation experiment, with a much closer intensity in the north and over the Shandong Peninsula and basically correct location and intensity of precipitation near the squall line. Moreover, the forecast precipitation over the Shandong Peninsula and Rizhao area is also accurate (Fig. 19b).

Fig. 17. Hourly surface precipitation (mm) observation during (a) 0800–0900 and (b) 0900–1000 BT 12 July 2005.
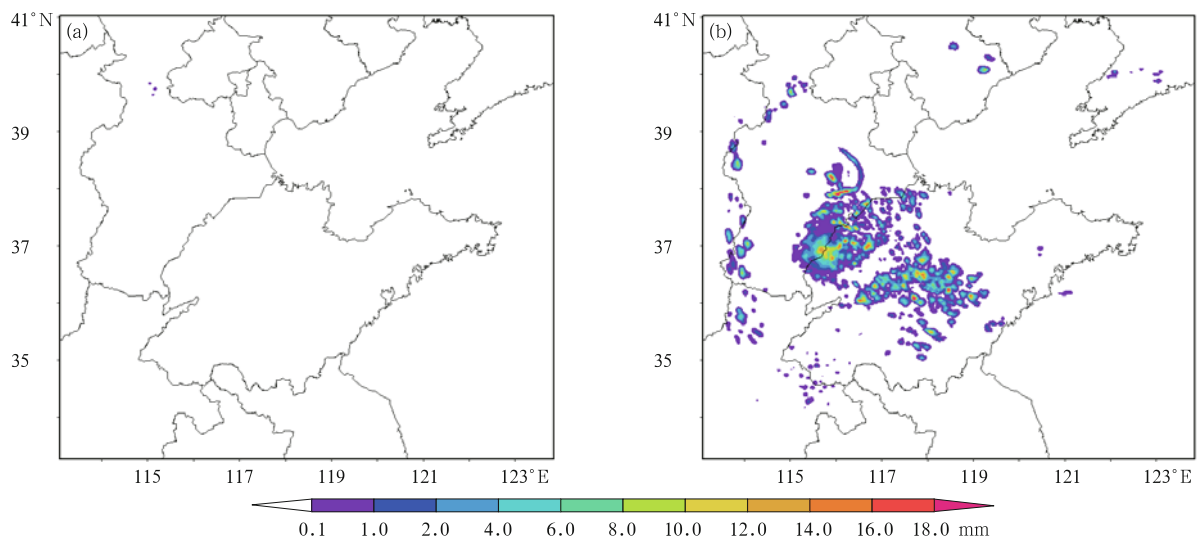
Fig. 18. Accumulated precipitation (mm) from (a) control run and (b) assimilation experiment during 0800–0930 BT 12 July 2005.

Fig. 19. Accumulated precipitation (mm) of (a) observation, (b) forecast by the control run, and (c) forecast by the assimilation experiment during 0800–2000 BT 12 July 2005.

7. Summary

This study explores the potential of using En-SRF to assimilate real radar data on convective scale through a squall line case study in midwest Shandong Province by employing the WRF model. Assessment is made using a variety of observations such as radar data, satellite data, and precipitation data. The experimental results show that:

(1) The EnSRF system demonstrates great promise in assimilating real Doppler radar data to initiate the convective squall line. Through radar data assimilation every 30 min, the convective-scale information is added into the high-resolution nonhydrostatic numerical model, and accurate and detailed structures of wind field, such as low-level cyclonic wind shear, severe wind region, and low-level wind convergence, can be analyzed effectively. Microphysical fields can also been retrieved accurately. The model spin-up time has been shortened, and the forecast of precipitation has been improved accordingly.

(2) Deterministic forecast initiated with the ensemble mean analysis of the 3rd assimilation cycle is performed. Compared with forecast of control run, the deterministic forecast initiated from EnSRF analysis produces more accurate microphysical fields, especially for the first 3 h, probably owing to a more accurate initial condition. The predicted wind and thermal fields are also reasonable and have the typical characteristics of convective storms.

(3) The propagation direction of the squall line simulated by ensemble mean analysis is consistent with the observation, but the propagation speed is faster than the observed. Probably because of nonlinear development of the convective storm, the effective forecast time for the squall line is about 5–6 h.

In most cases, there are not only liquid phase hydrometeors (e.g., cloud water and rain water) but also ice phase hydrometeors (e.g., ice crystal, snow, graupel, and hail) in mesoscale and microscale convective systems, such as squall line, tornado, etc., with deep cloud height and cold cloud top temperature below 0℃ during their vigorous development period. The ice phase hydrometeors and their microphysical processes play an important role in the occurrence and development of convective systems. Radar reflectivity data include all information of liquid phase and ice phase hydrometeors. If only a simple cloud microphysical scheme without ice phase processes is employed in the numerical model, the actual state of hydrometeors in the atmosphere certainly cannot be correctly retrieved in the assimilation procedure. Furthermore, it would bring false information into the cloud fields, and have a negative effect on forecast performance of other variables. As discussed in Sections 6.1.2 and 6.2.1, mixing ratio of the analyzed and simulated hydrometeors at 500 hPa in the assimilation experiment is similar to that of the observation. At 500 hPa, it is ice phase hydrometeors such as snow and hail that make the greatest contribution to the total mixing ratio of hydrometeors. The good performance of the WRF model in analyzing and forecasting hydrometeor fields in both their distributions and magnitudes for the studied squall line case is closely related to the accurate analysis of ice phase hydrometeors by the assimilation scheme when assimilating radar reflectivity data, as well as to the complicated cloud scheme used in the forecast model which includes ice phase microphysical processes.

Compared with OSSEs, in which the forecast model is assumed to be perfect, assimilation of real radar data, is much difficult. A major issue is the presence of model errors, which might be caused by model deficiencies in numerical discretization, micro-physical parameterization, lateral boundary condition, and so on, and might as well be caused by observation operators. On convective scale, microphysical parameterization might be the main source of model uncertainties. Further investigation should be performed by applying multiple microphysical schemes to different ensemble members to assess this kind of errors. Numerical discretization in space is another source of model errors. This can be partially alleviated by using higher resolutions. To solve the problem of filter divergence caused by model errors, adjustment of covariance inflation might be a simple while effective way in practice. This technique has been used in this study, and could be improved by making it adjustable in each EnSRF analysis so that ensemble spread could be adjusted automatically to best represent errors of the ensemble mean.

There are many different approaches to generating initial perturbations for ensemble-based assimilation schemes. The analyses and forecasts can be affected by uncertainties in many ways in the assimilation of real radar data. Proper initial perturbation can reduce the uncertainties in the environmental condition. In this study, the WRF 3DVAR system is used to generate a largely geostrophic balanced initial ensemble, while variables in a convective-scale system are highly ageostrophic; therefore, attempts to generate an initial ensemble suitable for convective-scale systems might have positive effects to some extent.

Observations obtainable for verification include soundings, synoptic data, automatic station data, and satellite data, of which the space and time resolution are not high enough to describe convective storms in detail. Although radar observations, which have sufficient resolutions, are also used for verification in this study, observations detected by radar are not model variables, so verification is somewhat difficult. Moreover, observation itself has errors, which also contributes to the uncertainties of verification of the EnSRF performance in assimilating real radar data.

REFERENCES

Dowell, D., F. Zhang, L. Wicker, et al., 2004: Wind and

temperature retrievals in the 17 May 1981 Arcadia, Oklahoma supercell: Ensemble Kalman filter experiments. *Mon. Wea. Rev.*, **132**, 1982–2005.

Evensen, G., 1994: Sequential data assimilation with a nonlinear quasi-geostrophic model using Monte Carlo methods to forecast error statistics. *J. Geophys. Res.*, **99**(C5), 10143–10162.

Gal-Chen, T., 1978: A method for the initialization of the anelastic equations: Implications for matching models with observations. *Mon. Wea. Rev.*, **106**, 587–602.

Gaspari, G., and S. Cohn, 1999: Construction of correlation functions in two and three dimensions. *Quart. J. Roy. Meteor. Soc.*, **125**, 723–757.

Hane, C., and P. Ray, 1985: Pressure and buoyancy fields derived from Doppler radar data in a tornadic thunderstorm. *J. Atmos. Sci.*, **42**, 18–35.

Hong, S., J. Dudhia, and S. Chen, 2004: A revised approach to ice microphysical processes for the bulk parameterization of clouds and precipitation. *Mon. Wea. Rev.*, **132**, 103–120.

Houtekamer, P., and H. Mitchell, 1998: Data assimilation using an ensemble Kalman filter technique. *Mon. Wea. Rev.*, **126**, 796–811.

——, and ——, 2001: A sequential ensemble Kalman filter for atmospheric data assimilation. *Mon. Wea. Rev.*, **129**, 123–137.

Hu Zhijin, Lou Xiaofeng, Bao Shaowu, et al., 1998: A simplified explicit scheme of phase-mixed cloud and precipitation. *J. Appl. Meteor. Sci.*, **9**, 257–264. (in Chinese)

Jones, C., and B. Macpherson, 1997: A latent heat nudging scheme for the assimilation of precipitation data into an operational mesoscale model. *Meteor. Appl.*, **4**, 269–277.

Kain, J., and J. Fritsch, 1990: A one-dimensional entraining/detraining plume model and its application in convective parameterization. *J. Atmos. Sci.*, **47**, 2784–2802.

——, and ——, 1993: Convective parameterization for mesoscale models: The Kain-Fritcsh scheme. The Representation of Cumulus Convection in Numerical Models. Amer. Meteor. Soc., Monograph 84.

Lin, Y., R. Farley, and H. Orville, 1983: Bulk parameterization of the snow field in a cloud model. *J. Climate Appl. Meteor.*, **22**, 1065–1092.

Lin, Y., P. Ray, and K. Johnson, 1993: Initialization of a modeled convective storm using Doppler radar-derived fields. *Mon. Wea. Rev.*, **121**, 2757–2775.

Qin Yanyan, Gong Jiandong, and Li Zechun, 2012: Assimilation of Doppler radar observations with an ensemble Kalman filter: OSS experiments. *Meteor. Mon.*, **38**, 513–525. (in Chinese)

Smith, P., C. Myers, and H. Orville, 1975: Radar reflectivity factor calculations in numerical cloud models using bulk parameterization of precipitation. *J. Appl. Meteor.*, **14**, 1156–1165.

Snyder, C., and F. Zhang, 2003: Assimilation of simulated Doppler radar observations with an ensemble Kalman filter. *Mon. Wea. Rev.*, **131**, 1663–1677.

Sun, J., and N. Crook, 1997: Dynamical and microphysical retrieval from Doppler radar observations using a cloud model and its adjoint. Part I: Model development and simulated data experiments. *J. Atmos. Sci.*, **54**, 1642–1661.

Tong, M., and M. Xue, 2005: Ensemble Kalman filter assimilation of Doppler radar data with a compressible nonhydrostatic model: OSS experiments. *Mon. Wea. Rev.*, **133**, 1789–1807.

Whitaker, J., and T. Hamill, 2002: Ensemble data assimilation without perturbed observations. *Mon. Wea. Rev.*, **130**, 1913–1924.

Xiao Yanjiao, 2007: Three-dimensional multiple-radar reflectivity mosaics and its application study. Ph. D. dissertation, Nanjing University of Information Science & Technology, China, 128 pp.

Xu Daosheng, Shao Aimei, and Qiu Chongjian, 2012: Doppler radar data assimilation with a local SVD-En3DVar method. *Acta Meteor. Sinica*, **26**, 717–734, doi: 10.1007/s13351-012-0604-3.

Xu Xiaoyong, Zheng Guoguang, and Liu Liping, 2004: Dynamical and microphysical retrieval from simulated Doppler radar observations using the 4DVAR assimilation technique. *Acta. Meteor. Sinica*, **62**, 410–422. (in Chinese)

——, Liu Liping, and Zheng Guoguang, 2006: Numerical experiment of assimilation of Doppler radar data with an ensemble Kalman Filter. *Chinese J. Atmos. Sci.*, **30**, 712–728. (in Chinese)

Xue, M., D. Wang, D. Hou, et al., 1998: Prediction of the 7 May 1995 squall line over the central U. S. with intermittent data assimilation. Preprints, 12th Conference on Numerical Weather Prediction, Phoenix, AZ, 11–16 January, Amer. Meteor. Soc., 191–194.

——, M. Tong, and K. Droegemeier, 2006: An OSSE framework based on the ensemble square root Kalman filter for evaluating the impact of data from radar networks on thunderstorm analysis and forecasting. *J. Atmos. Ocean Technol.*, **23**, 46–66.

—— and Dong Jili, 2013: Assimilating best track minimum sea level pressure data together with Doppler radar data using an ensemble Kalman filter for Hurricane Ike (2008) at a cloud resolving resolution. *Acta Meteor. Sinica*, **27**, 379–399, doi: 10.1007/s13351-013-0304-7.

Yang Yanrong, Wang Zhenhui, Yang Hongping, et al., 2008: Doppler radar reflectivity and radial velocity data assimilation in numerical models. *Meteor. Mon.*, **34**, 26–34. (in Chinese)

Yang Yi, Qiu Chongjian, Gong Jiandong, et al, 2008: Study on Doppler weather radar data assimilation via 3D-Var. *Scientia Meteor. Sinica*, **28**, 124–132. (in Chinese)

——, Gong Zhongqiang, Wang Jinyan, et al., 2011: Time-expanded sampling approach for ensemble Kalman Filter: Experiment assimilation of simulated soundings. *Acta Meteor. Sinica*, **25**, 558–567, doi: 10.1007/s13351-011-0502-0.

Yu Xiaoding, Yao Xiuping, Xiong Tingnan, et al., 2006: *Principles and Applications of Doppler Weather Radar*. China Meteorological Press, Beijing, 314 pp. (in Chinese)

Zhang, J., F. Carr, and K. Brewster, 1998: ADAS cloud analysis. Preprints, 12th Conference on Numerical Weather Prediction, Phoenix, AZ, 11–16 January, Amer. Meteor. Soc., 185–188.

Zhang, F., C. and Snyder, J. Sun, 2004: Tests of an ensemble Kalman filter for convective-scale data assimilation: Impact of initial estimate and observations. *Mon. Wea. Rev.*, **132**, 1238–1253.

——, Z. Meng, and A. Aksoy, 2006: Tests of an ensemble Kalman filter for mesoscale and regional-scale data assimilation. Part I: Perfect model experiments. *Mon. Wea. Rev.*, **134**, 722–736.